PERGAMON

Magnetic and inelastic neutron scattering studies of a frustrated tetranuclear Mn^{3+} butterfly-type cluster

R. Basler [a], G. Chaboussant [a,*], C. Cañada-Vilalta [b], G. Christou [b], H. Mutka [c], S. Janssen [d], F. Altorfer [d], H.-U. Güdel [a]

[a] *Department of Chemistry and Biochemistry, University of Bern, CH-3000 Bern 9, Switzerland*
[b] *Department of Chemistry, University of Florida, Gainesville, FL 32611-7200, USA*
[c] *Institut Laue-Langevin, B.P. 156, F-38042 Grenoble Cedex 9, France*
[d] *Laboratory for Neutron Scattering, PSI and ETHZ, CH-5232 Villigen, Switzerland*

Received 5 November 2002; accepted 4 January 2003

Abstract

We report on the magnetic properties of the tetranuclear metallic cluster $[Mn_4O_2(O_2CPh)_6(dpm)_2]$. Using susceptibility, magnetization and inelastic neutron scattering (INS) spectroscopy we have determined the exchange and anisotropy parameters. The four Mn^{3+} ($S = 2$) form a tetranuclear cluster with butterfly-type geometry. The two core Mn^{3+} ions are strongly antiferromagnetically coupled with $J_b = -4.8 \pm 0.1$ meV. The outer Mn^{3+} ions are loosely coupled to the core spins via two different weak interactions, ferromagnetic and antiferromagnetic, respectively: $J_{w1} = +0.1 \pm 0.01$ meV and $J_{w2} = -0.1 \pm 0.01$ meV. In addition, the octahedrally coordinated outer Mn^{3+} ions experience a large single-ion anisotropy DS_z^2 with $D = -0.47 \pm 0.01$ meV due to a strong distortion of the MnO_6 octahedra. The Landé g-factor is $g = 1.94 \pm 0.03$. Frustration effects and competitive interactions lead to remarkable magnetic properties which cannot be unambiguously interpreted without the additional information from INS.
© 2003 Elsevier Science Ltd. All rights reserved.

Keywords: Tetranuclear cluster; Inelastic neutron scattering; Magnetic anisotropy; Susceptibility; Magnetic frustration

1. Introduction

The topic of molecular magnets has emerged in the last decade as one of the major interdisciplinary fields of research for the material sciences community. Chemists and physicists, experimentalists and theoreticians, have joined in an increasingly coordinated effort to develop and design new magnetic molecules that can show pure quantum properties at the macroscopic level [1,2]. Such phenomena include quantum tunneling of the magnetization vector through an energy barrier $\Delta \approx DS^2$ between 'spin up' and 'spin down' configurations but also very slow relaxation of the magnetization below the so-called 'blocking' temperature [3,4]. Beyond basic research motivations, one could foresee potential applications ranging from magnetic recording devices to

'quantum bits' technology [5,6]. Presently, the number of existing molecular magnets that display these properties is relatively scarce due to the serendipitous nature of the synthesis of new compounds. A wide range of experimental strategies, including specific heat [7], low-temperature magnetization [8,9], high-field EPR [10] and inelastic neutron scattering (INS) [11], is being used to determine the driving forces responsible for these remarkable properties and to feed back this essential information into the synthetic work.

In this context, one of the most versatile elements for the synthesis of compounds with interesting magnetic properties is manganese. Its main advantages are its accessibility in a number of oxidation states, as well as its magnetic anisotropy. The Mn^{3+} ion in particular is strongly anisotropic in an octahedrally coordinated environment, due to Jahn-Teller distortion of the MnO_6 octahedra. The study of manganese compounds has also been largely stimulated by the search of models

for Mn-containing proteins and enzymes [12]. For instance, a tetranuclear manganese cluster is known to be responsible for the oxidation of water into dioxygen in the photosystem II of green plants and cyanobacteria [13]. The exact structure of this complex remains unknown. In the absence of well resolved X-ray diffraction data, the main source of information about the cluster comes from the comparison of its physical properties with those of well characterized inorganic models. This has therefore been another incentive for the exploration of Mn clusters using different methods, including the other techniques mentioned above.

We have undertaken the study of a new molecular magnetic cluster that consists of four Mn^{3+} centers ($S = 2$) arranged in the so-called butterfly geometry. Several such butterfly-type clusters have been reported in the recent years such as Mn_4^{3+} [14–16], ($Mn_3^{3+}:Mn^{2+}$) [17], ($Mn_2^{3+}:Mn_2^{2+}$) [18] and Ni_4^{2+} [19,20]. The interest resides in understanding the magneto-structural correlations that control the magnetic properties of such spin clusters and, especially, their anisotropy.

The paper is organised as follows: The first section is dedicated to experimental details including structural characteristics of the title compound and experimental conditions, the second section summarizes the main experimental results (bulk magnetic measurements and INS), and in the third section we propose an analysis and a discussion based on our findings.

2. Experimental

2.1. Structural description of $[Mn_4O_2(O_2CPh)_6(dpm)_2]$

A polycrystalline sample of $[Mn_4O_2(O_2CPh)_6(dpm)_2]$ was prepared as described in Ref. [21]. The structure of $[Mn_4O_2(O_2CPh)_6(dpm)_2]$ is shown is Fig. 1(a), where a view down the crystallographic $\vec{c}$ axis is presented. Fig. 1(b) depicts a schematic drawing of the magnetic exchange pathways in the $[Mn_4O_2(O_2CPh)_6(dpm)_2]$ cluster. The central $[Mn_4O_2]^{8+}$ core has crystallographic C_2 symmetry and consists of 4 Mn^{3+} ($S = 2$) ions arranged in the so-called 'butterfly'-type geometry where two five-coordinated Mn ions makes up the 'body' and two six-coordinated Mn ions, the outer or 'wingtip' sites, are located on each side of the core. Each outer Mn ion is bridged to the two central Mn ions through μ_3-oxo and benzoate bridges. Two chelating dpm$^-$ groups complete the ligation on the wingtip ions. The local oxygen environment of the two central Mn^{3+} ions is that of a square pyramid while it is a distorted octahedral geometry for the outer Mn^{3+} centers. More detailed synthetic and structural information can be found in Ref. [21]. The polycrystalline sample was additionally characterized by powder X-ray diffraction.
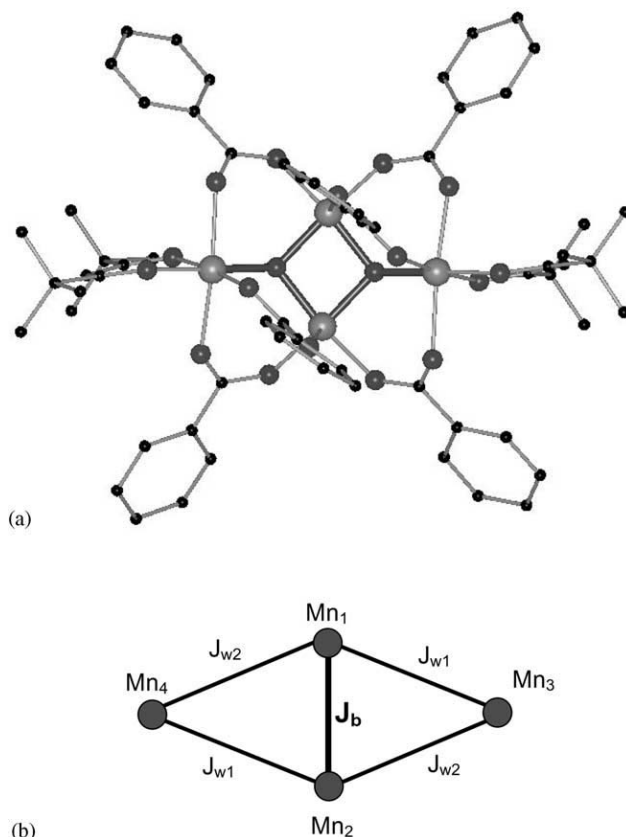

Fig. 1. (a) Structure of $[Mn_4O_2(O_2CPh)_6(dpm)_2]$ view along the $\vec{c}$-axis. Large solid spheres represent Mn^{3+} ions. Outer Mn ions have a distorted octahedral coordination geometry. (b) Schematic drawing of the Mn$_4$ cluster and magnetic exchange pathways as disscussed in the text.

Theoretical powder X-ray patterns were calculated using the program WINXPOW on the basis of the single crystal X-ray data. The measured powder pattern matched the calculated one.

2.2. Experimental methods

Susceptibility and magnetization measurements were carried out at variable temperatures and fields, covering the temperature range of 1.8–300 K at 0.1 T, and a field range of 0–5 T, respectively. The measurements were performed on a Quantum MPMS XL-5 magnetometer. The samples were sealed in a eicosane matrix to prevent torquing under the magnetic field. The data were corrected for the diamagnetic contribution, which was estimated from Pascal's constants ($\chi_{dia} \approx -7.34 \times 10^{-4}$ emu mol^{-1}). For all INS experiments, the polycrystalline samples were filled under Helium into a rectangular flat Aluminum slab container of 3 mm thickness with dimensions 20×30 mm. The INS experiments were performed on the time-of-flight spectrometer IN6 at the Institut Laue-Langevin (ILL, France) using cold neutrons of wavelength $\lambda = 4.1$ Å and on the time-of-flight

spectrometer FOCUS at the Paul-Scherrer Institute (PSI, Switzerland) using cold neutrons of wavelength $\lambda = 4.3$ and 5.8 Å. The ^{3}He detector banks covered a wide angular range, $2\theta = 10{-}114°$ for IN6 and $2\theta = 10{-}130°$ for FOCUS. This gave access to a large range of momentum transfer Q. Data were collected at several temperatures between 1.5 and 30 K and corrected for the background and detector efficiency by means of the spectrum of an empty container and Vanadium metal, respectively. Data reduction was performed using the programs INX (ILL data) and NINX (PSI data). All magnetic and INS calculations were carried out using the program MAGPACK [22], which is based on the general numerical formalism for solving spin cluster problems developed in Ref. [23]. Least-squares fits were based on the Levenberg-Marquart method in combination with MAGPACK.

3. Experimental results

3.1. Susceptibility and magnetization measurements

Fig. 2(a) shows the magnetic susceptibility measured at a DC field of 0.1 T and presented as the product χT versus T. χT does not saturate even at room temperature since the expected value for a truly paramagnetic regime is $\chi T \approx N\mu_B^2/3k_B g^2 nS(S+1)$. With $g = 1.94$, $n = 4$ and $S = 2$, one obtains $\chi T \approx 11.3$ emu K mol^{-1}. This is far above the experimentally observed value. In addition, the constant decrease of the χT product between 300 and 25 K is indicative of strong antiferromagnetic (AFM) exchange interactions within the cluster. A sharp downturn is observed below 20 K. This behaviour is primarily due to the characteristically strong single-ion anisotropy of Mn^{3+} ions (see below). The inset shows a close-up look at the low-temperature regime. Fig. 2(b) shows the low-temperature magnetization curve $M(H)$ obtained at 1.8 K. $M(H)$ progressively increases with increasing fields but does not saturate. The observed magnetization value at 5 T is $M/N\mu_B \approx 5{-}6$.

3.2. Inelastic neutron scattering

Fig. 3 shows a low-temperature (1.4 K) INS spectrum obtained on FOCUS at $\lambda = 5.8$ Å. The elastic resolution is FWHM ≈ 0.055 meV (Full Width at Half-Maximum). The average Q value is around 1.1 Å^{-1}. No evidence for magnetic scattering can be found between 0.2 and 1.2 meV. Fig. 4 shows different spectra obtained on FOCUS at $\lambda = 4.3$ Å (top) and on IN6 at $\lambda = 4.1$ Å (bottom). The elastic resolution in both setups is FWHM $\approx 0.15{-}0.17$ meV. Data at different temperatures have been shifted vertically for clarity. Positive (negative) energy transfers correspond to neutron en-
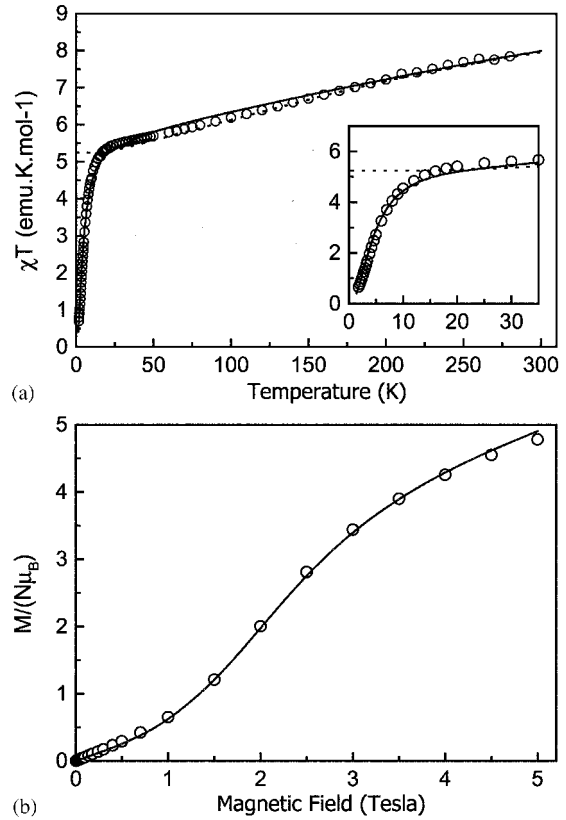

Fig. 2. (a) Magnetic susceptibility measured under a static magnetic field of $H = 0.1$ T. (b) Magnetization curve at $T = 1.8$ K. In both panels, continuous lines are calculated curves based on the model discussed in the text. The best fit to the susceptibility and magnetization data was obtained for $J_b = -4.80 \pm 0.10$ meV, $J_{w1} = +0.10 \pm 0.002$ meV, $J_{w2} = -0.10 \pm 0.002$ meV, $D = -0.47 \pm 0.01$ meV and $g = 1.94 \pm 0.03$. The dotted line corresponds to the parameters proposed in Ref. [21]; $J_b = -3.35$ meV, $J_w = J_{w1} = J_{w2} = -0.05$ meV and $g = 1.87$.
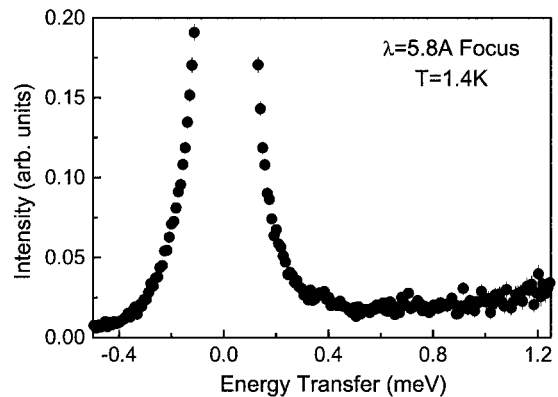

Fig. 3. INS spectra at $\lambda = 5.8$ Å obtained on FOCUS at $T = 1.4$ K. All detectors were grouped together ($10 \leq 2\theta \leq 130°$) leading to an average vector Q between 1.0 and 1.2 Å^{-1}.

ergy loss (gain), respectively. On the loss side several peaks are observed between 0.5 and 3 meV whose origin can be interpreted as follows:
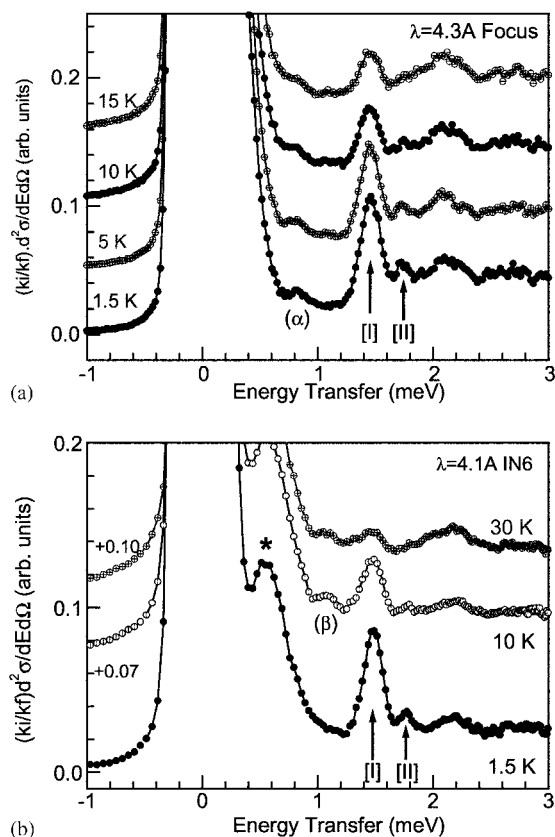
Fig. 4. (a) INS spectra at $\lambda = 4.3$ Å obtained on FOCUS at different temperatures. All detectors were grouped together ($10 \leq 2\theta \leq 130°$). (b) INS spectra at $\lambda = 4.1$ Å obtained on IN6 at different temperatures. Low-angle detectors were grouped together leading to an averaged angle $2\theta = 40.4°$. The Q values are in a range where magnetic scattering is usually the strongest: $Q \approx 1.0$–1.5 Å.

a) In both spectra (FOCUS and IN6) there is a prominent peak centered at $\hbar\omega \approx 1.50$ meV, labeled (I), for which the integrated intensity decreases steadily when the temperature is increased from 1.5 to 30 K. There is also a smaller peak at $\hbar\omega \approx 1.75$ meV, labeled (II), whose temperature dependence is similar to that of peak (I). Their behaviour strongly suggest a magnetic origin for transitions (I) and (II).

b) The small scattering at $\hbar\omega \approx 0.75$ meV (labeled α) on FOCUS is absent in the $\lambda = 5.8$ Å data, shown in Fig. 3, suggesting a spurious origin.

c) The broad peak at $\hbar\omega \approx 0.55$ meV, marked with an asterisk (*), is only observed on IN6 and it is a known artefact due to Aluminum Bragg scattering that occurs specifically for $\lambda = 4.1$ Å.

d) On IN6, the small peak at $\hbar\omega \approx 1.1$ meV (labeled β) is seen neither in the $\lambda = 5.8$ Å data nor in the $\lambda = 4.3$ Å data of FOCUS. This is again a spurious peak.

e) At higher energies, several broad features are observed which are, on the basis of temperature and Q-dependence, attributed to phononic excita-

tions. The relative importance of spurious intensities and strong phonon background in these spectra is the result of the large number of hydrogen atoms in the sample, since hydrogen is a very strong incoherent scatterer. Deuteration is not reasonably achievable for the present material.

On the gain side in Fig. 4 broad peaks are observed around $\hbar\omega \approx -1.5$ and -2.2 meV (not shown) in both the IN6 and FOCUS data. However, the poor resolution (FHWM ≥ 0.3 meV) on the gain side makes it difficult to analyze. Fig. 5 shows a constant energy Q-scan at $\hbar\omega \approx 1.5$ meV, i.e. the position of peak (I), obtained on the triple-axis spectrometer Drüchal. There is a slight decrease of the intensity with increasing Q but no clear structure.

4. Analysis

To find the relevant magnetic model for this cluster, we ought first to consider the bond distances and angles between the Mn ions. Fig. 1(a) shows the Mn_4 cluster along the $\vec{c}$ axis. We adopt the following notation for the Mn ions: Mn_1 and Mn_2 represent the body (or central) sites while Mn_3 and Mn_4 are the outer sites as shown in Fig. 1(b). The main inter-atomic distances and bond angles are listed in Table 1. Considering the C_2 site symmetry of the cluster and the structural details described above, it is legitimate to consider three different exchange coupling constants J_b, J_{w1} and J_{w2}. These are depicted in Fig. 1(b). From these standard magneto-structural considerations, the effective magnetic Hamiltonian based on the coupling scheme shown in Fig. 1(b), including single-ion anisotropy, is written as
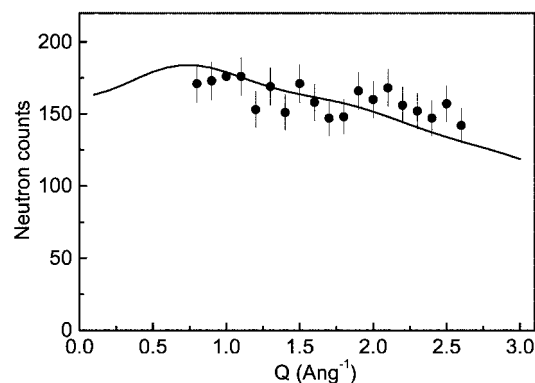

Fig. 5. Q-dependence of peak (I) at $\hbar\omega \approx 1.50$ meV measured at 1.5 K on the triple-axis spectrometer Drüchal (PSI, Switzerland) with final energy $E_f = 4.5$ meV. The solid line is a calculation based on Eq. (1) with $J_b = -4.80$ meV, $J_{w1} = +0.10$ meV, $J_{w2} = -0.10$ meV and $D = -0.47$ meV.

Table 1
Main inter-ionic distances $Mn_i–Mn_j$ and bond angles $Mn_i–O_x–Mn_j$ in the title compound

Mn(III) ion label		Inter-ionic distance (Å)	Bond angles (°)	
i	j		δ ($Mn_i–O_1–Mn_j$)	δ ($Mn_i–O_2–Mn_j$)
Mn_1	Mn_2	2.841	98.5	98.5
Mn_1	Mn_3	3.255	120.1	
Mn_1	Mn_4	3.362		125.9
Mn_2	Mn_3	3.362	125.9	
Mn_2	Mn_4	3.255		120.1

The numbering scheme refers to the labeling in Fig. 1(b).

$$\mathscr{H}_1 = -2J_b\hat{\vec{S}}_1 \cdot \hat{\vec{S}}_2 - 2J_{w1}(\hat{\vec{S}}_1 \cdot \hat{\vec{S}}_3 + \hat{\vec{S}}_2 \cdot \hat{\vec{S}}_4)$$
$$- 2J_{w2}(\hat{\vec{S}}_1 \cdot \hat{\vec{S}}_4 + \hat{\vec{S}}_2 \cdot \hat{\vec{S}}_3) + \mathscr{H}_{ani} \qquad (1)$$

where negative exchange parameters represent AFM interactions and

$$\mathscr{H}_{ani} = \sum_{i=1}^{4} D_i \hat{S}_{i,z}^2 \qquad (2)$$

is the axial single-ion anisotropy term known to be significant for Mn^{3+} ions. By interchanging J_{w1} and J_{w2} in Eq. (1) we would get an equivalent Hamiltonian. We cannot distinguish between the two possibilities.

First we consider the isotropic symmetric case: $D_i = 0$ and $J_{w1} = J_{w2} = J_w$. The energy level scheme is then straightforward: Neglecting the constant terms and with the intermediate spins $\vec{S}_{12} = \vec{S}_1 + \vec{S}_2$ and $\vec{S}_{34} = \vec{S}_3 + \vec{S}_4$ and total spin $\vec{S} = \vec{S}_{12} + \vec{S}_{34}$, Eq. (1) becomes:

$$\mathscr{H}_1 = -J_b\vec{S}_{12}^2 - J_w(\vec{S}^2 - \vec{S}_{12}^2 - \vec{S}_{34}^2) \qquad (3)$$

and the energy levels for the states $|S, S_{12}, S_{34}\rangle$ are given by:

$$\begin{aligned} E(S, &\ S_{12},\ S_{34}) \\ &= -J_b S_{12}(S_{12}+1) \\ &\quad - J_w[S(S+1) - S_{12}(S_{12}+1) - S_{34}(S_{34}+1)] \end{aligned} \qquad (4)$$

where $S_1 = S_2 = S_3 = S_4 = 2$, $0 \leq S_{12} \leq 4$, $0 \leq S_{34} \leq 4$ and $|S_{12} - S_{34}| \leq S \leq S_{12} + S_{34}$.

On the basis of the magnetic susceptibility measurements between 25 and 300 K, Cañada-Vilalta et al. [21] estimated the exchange couplings based on this isotropic ($D_i = 0$) symmetric ($J_{w1} = J_{w2} = J_w$) model. They obtained a best fit to the data with the following set of parameters: $J_b \approx -3.35$ meV, $J_w = -0.05$ meV and the Landé factor $g = 1.87$. The AFM body interaction, J_b, is by far the strongest exchange coupling in this cluster. The approximation $J_{w1} = J_{w2}$ was justified in that study considering the temperature range used to derive the exchange couplings ($T_{min} \approx 25$ K $\gg J_w$). With the dominant AFM coupling J_b, the core dimer $Mn_1–Mn_2$ is firmly in a singlet state ($S_{12} = 0$) at low-temperatures,

and the outer spins S_3 and S_4 are largely decoupled. Thus, the ground state is fivefold degenerate since all the states with $S_{12} = 0$ and $S_{34} = S = 0, 1, 2, 3, 4$ have the same, lowest energy. This high degeneracy of the ground state constitutes a clear case of a frustrated system [28]. Fig. 2(a) compares our experimental χT product with the simulated curve obtained using the parameters proposed in Ref. [21] (dotted line). The agreement is good down to $T \approx 20–25$ K but the observed low-temperature downturn, see inset of Fig. 2(a), is not accounted for by this model.

The model presented in Eq. (3) also fails to explain the INS data. Using the parameters proposed in Ref. [21], energy levels can easily be calculated using Eq. (4). Magnetic INS experiments measure directly the differential magnetic cross-section for a transition between initial state Ψ_n and final state Ψ_{nm} is given by [24]:

$$\begin{aligned} \frac{d^2\sigma}{d\Omega dE} &= \frac{N}{4}\left(\frac{\gamma_N r_e}{2}\right)^2 \frac{\vec{k}'}{\vec{k}} e^{-2W(Q,T)} \times \sum_{\alpha,\beta}\left(\delta_{\alpha,\beta} - \frac{Q_\alpha Q_\beta}{Q^2}\right) \\ &\quad \times \sum_{i,j}\{g_i F_i(Q)\}\{g_j F_j(Q)\} \\ &\quad \times e^{-i\vec{Q}(\vec{R}_i - \vec{R}_j)} p_m \langle\Psi_n|S_i^\alpha|\Psi_m\rangle\langle\Psi_m|S_j^\beta|\Psi_n\rangle \\ &\quad \times \delta(\hbar\omega + E_n - E_m) \end{aligned} \qquad (5)$$

where N is the number of magnetic centres in the sample, $(\gamma_N r_e/2)^2 = 0.294$ barn/Steradian, $\vec{k}$ and $\vec{k}'$ are the initial and final neutron wave-vectors and $\vec{Q} = \vec{k} - \vec{k}'$ is the scattering vector, $\exp(-2W)$ is the Debye-Waller factor, g_i is the Landé g-factor and $F_i(Q)$ is the magnetic form factor of the ith Mn^{3+}, Ψ_n is the wavefunction of cluster state n with energy E_n, $\vec{R}_i$ is the position of the ith Mn^{3+} ion in the cluster, α and β are the cartesian coordinates x, y and z, $\hbar\omega$ is the energy transferred to/from the neutron through the scattering process and p_n is the Boltzmann factor for the initial state Ψ_n. In most instances, matrix elements of the type $\langle\Psi_n|S_i^\alpha|\Psi_m\rangle$ have to be evaluated numerically.

According to the INS selection rules only transitions $|S, M\rangle \rightarrow |S', M'\rangle$ between cluster states that fulfill the following conditions have non-zero intensity

$$\Delta S = S' - S = 0, \pm 1$$

$$\Delta M = M' - M = 0, \pm 1 \qquad (6)$$

These selection rules are sufficient only in the case of a dimer cluster [25]. For tetranuclear clusters like [Mn₄O₂(O₂CPh)₆(dpm)₂] the following additional selection rules apply. (1) $\Delta S_{12} = 0, \pm 1$ and $\Delta S_{34} = 0$ and (2) $\Delta S_{34} = 0, \pm 1$ and $\Delta S_{12} = 0$. Consequently, transitions with both $\Delta S_{12} = \pm 1$ and $\Delta S_{34} = \pm 1$ are not allowed [20,26].

Fig. 6 shows both the energy level diagram (restricted to the $S_{12} = 0, 1, 2$ sectors) and the INS spectrum
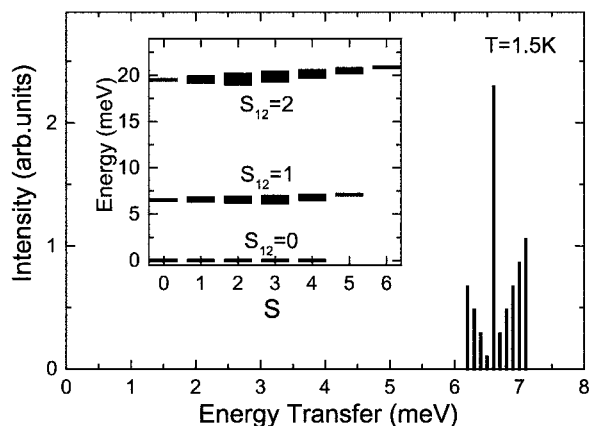
Fig. 6. Calculated INS spectrum at 1.5 K and energy levels obtained with the parameters from Ref. [21]: $J_b = -3.35$ meV and $J_w = J_{w1} = J_{w2} = -0.05$ meV.

calculated at $T = 1.5$ K and $Q \approx 1$ Å^{-1} for the isotropic symmetric model with $D_i = 0$ and $J_{w1} = J_{w2}$. The energy level diagram shows the highly degenerate ground state ($S = 0, 1, 2, 3, 4$) and two bands of excited states. The first excited states above the ground state have $S_{12} = 1$ and $S_{34} = 0, 1, 2, 3, 4$ with energies ranging between $-2J_b + 10J_w \approx 6.3$ meV ($S = 3$) and $-2J_b - 8J_w \approx 7.2$ meV ($S = 5$), while the second band corresponds to $S_{12} = 2$ with an average energy $6J_b \approx 20.1$ meV. The 'breadth' of the bands is solely controlled by J_w. At 1.5 K, inelastic transitions can occur between the degenerate ground states and the first band of excited states (with the selection rules discussed above). The low-temperature simulated INS spectrum shows a series of transitions between 6.2 and 7.2 meV. In the present experiments, we do not have access to such energy transfers, but it is obvious that the dominant observed magnetic peak (I) at $\hbar\omega \approx 1.50$ meV is not accounted for. We conclude that the simple model of Eq. (3) proposed in Ref. [21] is not appropriate or incomplete for the interpretation of the INS data.

There are two difficulties that arise in the analysis of the present set of magnetic data. First, a true paramagnetic regime is not attained even at room temperature. It means in particular that the Landé g factor cannot be determined *independently* from the main exchange parameter J_b. The larger g, the larger J_b has to be account for the data above 50 K. In other words, the parameters g and J_b are correlated. We find a good agreement to the susceptibility data with $J_b = -4.8$ meV and $g = 1.94$. The second difficulty is the low-temperature regime. Only the introduction of single-ion anisotropy (D_i) *and* inequivalent wing-body couplings ($J_{w1} \neq J_{w2}$) can explain the sharp downturn below $T \approx 20$ K. We find that, from magnetization and susceptibility alone, it is impossible to determine the values of all parameters unequivocally.

Inequivalent wing-body couplings can be rationalized by the different bridging angles and distances along $Mn_1 - Mn_3$ and $Mn_2 - Mn_3$, see Table 1. The need to consider single-ion anisotropy is borne out by the fact that the outer Mn^{3+} sites, Mn_3 and Mn_4, are in an octahedrally distorted local environment which will favour strong single-ion anisotropy due to their Jahn-Teller nature. Since the spins S_1 and S_2 are quenched into a singlet $S_{12} = 0$ state, the terms that will contribute to the anisotropy of the cluster are the ones of Mn_3 and Mn_4, namely D_3 and D_4. D_1 and D_2 are likely to be non-zero as well but they will only marginally change the low-energy properties [27].

The JT axes for both Mn_3 and Mn_4 ions are considered to be roughly parallel [21]: $\vec{D}_3 = \vec{D}_4 = D$ (see Fig. 1), and one can write the axial anisotropy Hamiltonian of Eq. (2) as:

$$\mathcal{H}_{ani} = D(\hat{S}_{3,z}^2 + \hat{S}_{4,z}^2). \tag{7}$$

With this model, the ground state degeneracy of the cluster is lifted and the energy levels in the ground state are given by the eigenvalues of Eq. (7) in the basis $|M_3, M_4, M\rangle$. Here, M is the total projection along z of the system formed by *two uncoupled* $S = 2$ spins and is expressed in terms of the individual z-components as $M = M_3 + M_4$. For $D < 0$, the energy levels read as:

$$E(0, 0, 0) = +8|D|$$

$$E(0, 1, 1) = E(1, 0, 1) = +7|D|$$

$$E(1, 1, 2) = +6|D|$$

$$E(0, 2, 2) = E(2, 0, 2) = +4|D|$$

$$E(2, 1, 3) = E(1, 2, 3) = +3|D|$$

$$E(2, 2, 4) = 0 \tag{8}$$

This energy level diagram is shown on the left side of Fig. 8. This allows to attribute the neutron peak (I) observed at $\hbar\omega \approx 1.50$ meV to a transition from the lowest lying state to the first excited state *within* the split ground state. It means that $\hbar\omega \approx 1.50$ meV $\approx 3|D|$ with $D < 0$ and $\hbar\omega \approx 1.50$ meV $\approx D$ with $D > 0$. A value of D of about -0.5 meV seems more reasonable and an easy test shows that having $D \approx +1.5$ meV leads to a strong disagreement with the susceptibility and magnetization data. Therefore, we conclude that the observed neutron peak at $\hbar\omega \approx 1.50$ meV corresponds to a magnetic transition between the $M = 4$ and $M = 3$ states with energy $\hbar\omega = 3|D|$ (see Fig. 8). The single-ion anisotropy is then estimated to be close to $D \approx -0.5$ meV. This purely axial model does not explain the origin of peak (II). It will be discussed below.

In order to better explain both the INS spectra and the magnetic behaviour at low-temperature, the suscept-

ibility and magnetization data were fitted using an axial and aysmmetric model that includes five parameters: J_b, J_{w1}, J_{w2}, D and g.

At high-temperatures, J_b and g control the behaviour of χT (slope and absolute value); D is essentially defined by the INS data. J_{w1}, J_{w2} and D control the downturn of χT at low-temperatures. In the fitting procedure, we therefore constrained D to be close to the value derived from the INS data and J_b, J_{w1}, J_{w2} and g are free to float within reasonable boundaries. A very good agreement between the susceptibility, magnetization and INS data is found with the following set of parameters.

$$J_b = -4.8(1) \text{ meV} \quad J_{w1} = +0.10(1) \text{ meV}$$
$$J_{w2} = -0.10(1) \text{ meV} \quad D = -0.47(1) \text{ meV} \tag{9}$$
$$g = 1.94(3)$$

Calculated curves, χT and $M(H)$, obtained with these parameters are shown in Fig. 2 as solid lines. A comparison between experimental and simulated INS spectra (thick solid lines) using the parameters (Eq. (9)) is shown in Fig. 7 at two temperatures (1.5 and 10 K). Simulated spectra were shifted to account for the background (dashed line) and scaled to the data using only one adjustable parameter. The large magnetic peak (I) at $\hbar\omega \approx 1.50$ meV corresponds to the $\hbar\omega \approx 3D$ transition within the ground state. The weak neutron peak (II) observed at $\hbar\omega \approx 1.75$ meV can be rationalized by introducing a small rhombic term $E[(\hat{S}_{3,x}^2 - \hat{S}_{3,y}^2) + (\hat{S}_{4,x}^2 - \hat{S}_{4,y}^2)]$ in Eq. (7). The best agreement to the data is then found for $D \approx -0.48$ meV and $E \approx \pm 0.045$ meV. A simulated INS spectrum at 1.5 K corresponding to this refined model is shown in Fig. 7 (thin solid lines). Note that although the E term explains the position and

intensity of peak (II), we have ignored it in the analysis of the susceptibility and magnetization since it does not significantly alter the calculated curves. In other words, the E term is a marginal perturbation. At higher temperatures, hot transitions appear below 1.5 meV. The agreement with the neutron data is satisfactory. The observed Q-dependence of peak (I) is also well reproduced as shown in Fig. 5. The resulting energy levels using the final set of parameters (Eq. (9)) are shown in Fig. 8 (right part of the graph).

5. Discussion

Interestingly, the wing-body couplings J_{w1} and J_{w2} are several orders of magnitude smaller than either the body–body coupling J_b or the single-ion anisotropy D and can be considered, in first order, as a small perturbation. However, we found that inequivalent body–wing couplings ($J_{w1} \neq J_{w2}$) are necessary to explain the present set of data. Intuitively, and taking the isotropic limit $D = 0$, it is apparent that inequivalent
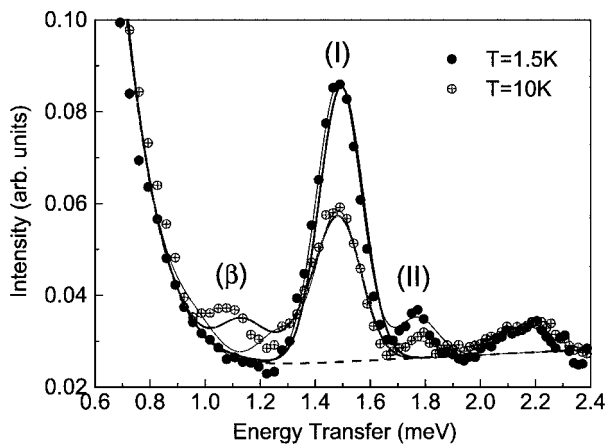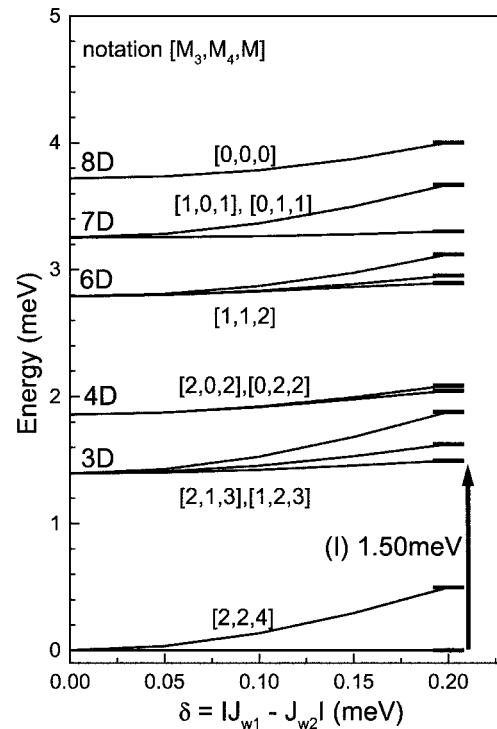

Fig. 7. Calculated INS spectra at 1.5 and 10 K with the parameters $J_b = -4.80$ meV, $J_{w1} = +0.10$ meV, $J_{w2} = -0.10$ meV, $D = 0.47$ meV (thick solid lines). For all transitions, a Gaussian line-shape is assumed with FWHM ≈ 0.17 meV (loss side). The dashed line represents a phenomenological background (linear slope+Gaussian decay). Thin solid lines are calculated INS spectra obtained by introducing a rhombic term $E \approx +0.045$ meV in the anisotropy. The weak peak (II) at $\hbar\omega = 1.75$ meV is then accounted for.

Fig. 8. Diagram of the low-energy levels restricted to the $S_{12} = 0$ sector. Stated are labeled in the basis $|M_3, M_4, M\rangle$. M is the total projection along z of the system made of *two uncoupled $S_3 = S_4 = 2$* spins: $M = M_3 + M_4$. The calculated energy levels are displayed as a function of $\delta = |J_{w1} - J_{w2}|$ with $J_b = -4.80$ meV, $J_{w1} = +0.10$ meV and $D = -0.47$ meV unchanged. The energy levels defined in Eq. (8) are recovered for $J_{w1} = J_{w2}$ (left hand side of the graph). The best agreement to the data is found for $|J_{w1} - J_{w2}| \approx +0.2$ meV (right hand side of the graph). The thick arrow indicates the INS transition corresponding to peak (I) with energy $\hbar\omega = 1.50$ meV.

couplings will remove part of the fivefold degeneracy described earlier and will favour a singlet ground state with $S_{12} = 0$ and $S = 0$. Note that in the case $J_{w1} \neq J_{w2}$, a Kambe coupling scheme is not possible and a full matrix diagonalization is required to obtain the eigenvalues. Alternatively, in the strongly anisotropic case ($D < 0$ and $|D| \gg |J_{w1}|$, $|J_{w2}|$), having inequivalent body–wing couplings will result in lifting the degeneracy of the M levels as shown in Fig. 8. The *necessity* to include inequivalent body–wing couplings is borne out by the fact that it explains quantitatively the susceptibility, magnetization and INS simultaneously.

The final set of parameters suggests that we also need the body–wing couplings to be (a) *opposite in sign* (one FM and one AFM) and (b) of *similar absolute magnitude*. One could argue that J_{w1} and J_{w2} are very small and therefore very difficult to determine from the present data. It turns out that the behaviour of the susceptibility is extremely sensitive to these couplings and having both couplings FM or both AFM leads to significantly poorer agreement with the data. This is clearly shown in Fig. 9 where the experimental χT curve is compared to several calculated curves for which only the parameters J_{w1} and J_{w2} are varied. For all curves in Fig. 9 the following parameters are kept unchanged: $J_b = -4.80$ meV, $g = 1.94$ and $D = -0.47$ meV. It is apparent that when $\delta = |J_{w1} - J_{w2}| \approx 0.2$ meV (see Fig. 9(a and b)) the agreement to the data is much better than when $\delta \approx 0.1$ or 0.4 meV (see Fig. 9(c)) or when
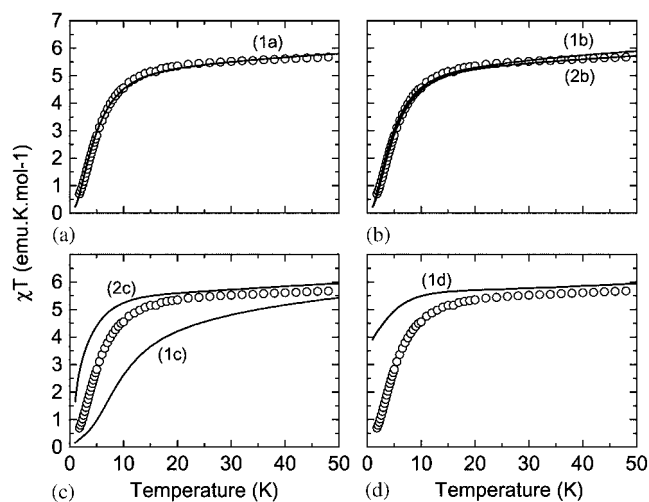
$\delta = 0$ (see Fig. 9(d)). From Fig. 9, one can see that the susceptibility (but also the magnetization) is sensitive not so much on the values of J_{w1} and J_{w2} but primarily on the absolute value of their difference $\delta = |J_{w1} - J_{w2}|$. The overall best agreement to the data shown in Fig. 9 is found for $J_{w1} \approx -J_{w2} \approx 0.1$ meV. We conclude that, according to the model developed in this article, J_{w1} and J_{w2} are of opposite sign and similar in absolute value. This conclusion is new in the butterfly-type Mn_4 cluster literature in which the symmetric approximation $J_{w1} = J_{w2}$ is the most common.

In recent studies of Mn_4 butterfly-type clusters, containing Mn^{3+} ions, it was reported that the body–wing coupling J_w is approximately one order of magnitude smaller than the body–body interaction J_b [15,16,14]. The impact of single-ion anisotropy is significant for Mn^{3+} ions (single-ion D of 0.1 to 1 meV are common) but is usually not addressed in the analysis of the susceptibility of these compounds [14,15,17] and this may lead to an inaccurate estimate of the exchange couplings. In this situation, it is important to consider magnetic data down to the lowest available temperatures. Next higher order terms like wing–wing interactions of the type $J_{ww}(\vec{S}_3 \cdot \vec{S}_4)$ can help improving the agreement to the data as shown in Ref. [14] but should be considered only after exhaustion of more relevant terms [17]. In parallel to the analysis of the susceptibility using an isotropic model, single-ion anisotropy is often included in the analysis of the low-temperature magnetization. If the anisotropy is very small compared to all the exchange couplings this may be a valid procedure. However, a more rigorous approach involves analyzing both the susceptibility *and* the magnetization with a model that includes single-ion anisotropy. The explicit inclusion of single-ion anisotropy in a frustrated Mn^{3+} butterfly-type cluster was considered by Libby et al. [16]. As in the title compound, they found that J_b was strongly AFM and also that a strong (positive in that case) single-ion anisotropy was required to explain the low-temperature downturn of the χT product.

6. Conclusions

We have shown for the butterfly-type spin cluster $[Mn_4O_2(O_2CPh)_6(dpm)_2]$ that an unambiguous determination of all the relevant interaction parameters on the basis of magnetic data alone is not possible when competition and/or frustration is at work. The intrinsic frustration generated by the regular butterfly-type geometry [28] is partially removed in the present system due to inequivalent body–wing couplings and single-ion anisotropy. Our work clearly shows that INS can bring crucial bits of information independently from bulk measurements. It is apparent that even a simple tetra-

Fig. 9. Comparison between the experimental χT product (shown also in Fig. 2) and calculated χT curves for different sets of parameters. For all curves, $J_b = -4.80$ meV, $g = 1.94$ and $D = -0.47$ meV. Each solid line is a calculated curve using different sets of J_{w1} and J_{w2}: (a) $J_{w1} = +0.1$ and $J_{w2} = -0.1$ for line (1a). (b) $J_{w1} = +0.0$ and $J_{w2} = +0.2$ for line (1b) and $J_{w1} = +0.0$ and $J_{w2} = -0.2$ for line (2b). The agreement to the data is good in both panels. (c) $J_{w1} = +0.2$ and $J_{w2} = 0.2$ for line (1c) and $J_{w1} = +0.0$ and $J_{w2} = +0.1$ for line (2c). (d) $J_w = J_{w1} = J_{w2}$ for line (1d), independent on the value of J_w. An identical curve is obtained for any value of J_w. Severe deviations from the data are observed in panels (c) and (d).

nuclear cluster can display magnetic properties which are not trivial to analyze due to competitive and frustration effects. INS is a unique and useful tool to unambiguously discriminate between different models and should serve as an ideal complementary technique to bulk thermodynamic measurements in the field of molecular clusters.

Acknowledgements

References

[1] R. Sessoli, D. Gatteschi, A. Caneschi, M.V. Novak, Nature 365 (1993) 141.

[2] D. Gatteschi, A. Caneschi, L. Pardi, R. Sessoli, Science 265 (1994) 1054.

[3] L. Thomas, F. Lionti, R. Ballou, D. Gatteschi, R. Sessoli, B. Barbara, Nature 383 (1996) 145.

[4] B. Barbara, I. Chiorescu, R. Giraud, A.G.M. Jansen, A. Caneschi, J. Phys. Soc. Jpn Suppl. A 69 (2000) 383.

[5] B. Barbara, L. Thomas, F. Lionti, I. Chiorescu, A. Sulpice, J. Mag. Magn. Mat. 200 (1999) 167.

[6] M.N. Leuenberger, D. Loss, Nature 410 (2001) 789.

[7] F. Luis, F.L. Mettes, J. Tejada, D. Gatteschi, L.J. de Jongh, Phys. Rev. Lett. 85 (2000) 4377.

[8] C. Sangregorio, T. Ohm, C. Paulsen, R. Sessoli, D. Gatteschi, Phys. Rev. Lett. 78 (1997) 4645.

[9] W. Wernsdorfer, R. Sessoli, Science 284 (1999) 133.

[10] A.L. Barra, D. Gatteschi, R. Sessoli, Phys. Rev. B 56 (1997) 8192.

[11] I. Mirebeau, M. Hennion, H. Casalta, H. Andres, H.-U. Güdel, A.V. Irodova, A. Caneschi, Phys. Rev. Lett. 83 (1999) 628.

[12] (a) K. Wieghardt, Angew. Chem., Int. Ed. Engl. 28 (1989) 1153;
(b) L. Que, A.E. True, Prog. Inorg. Chem. 38 (1990) 97;
(c) J.B. Vincent, G. Christou, Adv. Inorg. Chem. 33 (1989) 197;
(d) G. Christou, Acc. Chem. Res. 22 (1989) 328;
(e) V.L. Pecoraro (Ed.), Manganese Redox Enzymes, VCH Publishers, New York, 1992.

[13] V.K. Yachandra, K. Sauer, M.P. Klein, Chem. Rev. 96 (1996) 2927.

[14] G. Aromí, S. Bhaduri, P. Artús, J.C. Huffman, D.N. Hendrickson, G. Christou, Polyhedron 21 (2002) 1779.

[15] J.B. Vincent, C. Christmas, H.-R. Chang, Q. Li, P.D.W. Boyd, J.C. Huffman, D.N. Hendrickson, G. Christou, J. Am. Chem. Soc. 111 (1989) 2086.

[16] E. Libby, J.K. McCusker, E.A. Schmitt, K. Folting, D.N. Hendrickson, G. Christou, Inorg. Chem. 30 (1991) 3486.

[17] B. Albela, M.S. El Fallah, J. Ribas, K. Folting, G. Christou, D.N. Hendrickson, Inorg. Chem. 40 (2001) 1037.

[18] J. Yoo, E.K. Brechin, A. Yamaguchi, M. Nakano, J.C. Huffman, A.L. Maniero, L.C. Brunel, K. Awaga, H. Ishimoto, G. Christou, D.N. Hendrickson, Inorg. Chem. 39 (2000) 3615.

[19] A. Escuer, R. Vincente, S.B. Kumar, F.A. Mautner, J. Chem. Soc., Dalton Trans. 3473 (1998).

[20] J.M. Clemente-Juan, H. Andres, J.J. Borrá-Almenar, E. Coronado, H.-U. Güdel, M. Aebersold, G. Kearly, H. Büttner, M. Zolliker, J. Am. Chem. Soc. 121 (1999) 10021.

[21] C. Cañada-Vilalta, J.C. Huffman, G. Christou, Polyhedron 20 (2001) 1785.

[22] J.J. Borrás-Almenar, J.M. Clemente, E. Coronado, B.S. Tsukerblat, J. Comput. Chem. 22 (2001) 985.

[23] J.J. Borrás-Almenar, J.M. Clemente, E. Coronado, B.S. Tsukerblat, Inorg. Chem. 38 (1999) 6081.

[24] W. Marshall, S.W. Lovesey, Theory of Thermal Neutron Scattering, Clarendon press, Oxford, 1971.

[25] A. Furrer, H.-U. Güdel, J. Magn. Mat. Mat. 14 (1979) 256.

[26] H. Andres, J.M. Clemente-Juan, M. Aebersold, H.-U. Güdel, E. Coronado, H. Büttner, G. Kearly, J. Melero, R. Burriel, J. Am. Chem. Soc. 121 (1999) 10028.

[27] With $D_1 = D_2 = \pm 0.47$ meV the maximum shift of the energy levels (specially the ones at 1.495 meV) is less than 4.2%. The impact is therefore extremely limited and neglecting D_1 and D_2 is a reasonable simplication of the problem.

[28] O. Kahn, Molecular Magnetism, VCH Publishers, New York, 1993, pp. 244–245.